Tissue-Compliant Neural Implants from Microfabricated Carbon Nanotube Multilayer Composite

Huanan Zhang,[†] Paras R. Patel,[‡] Zhixing Xie,[§] Scott D. Swanson,[§] Xueding Wang,[‡,§] and Nicholas A. Kotov[†,‡,⊥,∥,*]

[†]Department of Chemical Engineering, [‡]Department of Biomedical Engineering, [§]Department of Radiology, [⊥]Department of Materials Science, and [∥]Biointerface Institute, University of Michigan, Ann Arbor, Michigan 48109, United States

ABSTRACT Current neural prosthetic devices (NPDs) induce chronic inflammation due to complex mechanical and biological reactions related, in part, to staggering discrepancies of mechanical properties with neural tissue. Relatively large size of the implants and traumas to blood-brain barrier contribute to inflammation reactions, as well. Mitigation of these problems and the realization of long-term brain interface require a new generation of NPDs fabricated from flexible materials compliant with the brain tissue. However, such materials will need to display hard-to-combine mechanical and electrical properties which are not available in the toolbox of classical neurotechnology. Moreover, these new materials will concomitantly demand different methods of (a) device micromanufacturing and (b) surgical implantation in brains because currently used processes take advantage of high stiffness of the devices. Carbon nanotubes (CNTs) serve as a promising foundation for such materials because of their record mechanical and electrical properties, but CNT-based tissue-compliant devices have not been realized yet. In this study, we formalize the mechanical requirements to tissue-compliant implants based on critical rupture strength of brain tissue and demonstrate that miniature CNT-based devices can satisfy these requirements. We fabricated them using MEMS-like technology and miniaturized them so that at least two dimensions of the electrodes would be comparable to brain tissue cells. The nanocomposite-based flexible neural electrodes were implanted into the rat motor cortex using a surgical procedure specifically designed for soft tissue-compliant implants. The post-surgery implant localization in the motor cortex was successfully visualized with magnetic resonance and photoacoustic imaging. *In vivo* functionality was demonstrated by successful registration of the low-frequency neural recording in the live brain of anesthetized rats. Investigation of inflammation processes around these electrodes will be required to establish their prospects as long-term neural electrodes.

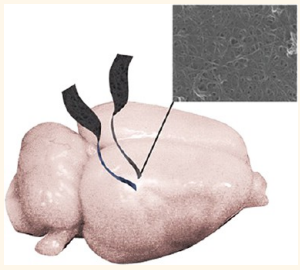

KEYWORDS: flexible neural prosthetic electrode · nanocomposite · carbon nanotube · layer-by-layer assembly · MEMS · photoacoustic microscopy · magnetic resonance imaging · tissue-compliant electrodes

Implantable neural prosthetic devices (NPDs) have attracted considerable attention in the field of fundamental and clinical neuroscience research. They can potentially transform the treatments and diagnostics of many neurological disorders and traumas.[1−3] Furthermore, NPDs are the central technological component for advances toward a functional brain−computer interface.[4] Classical NPDs being used to record or stimulate neural cells, especially in the clinical setting, are typically noble metal microwires with diameters of 50 to 200 μm.[5,6] Recently, improvements in neural electrode research have been centered around silicon-based microfabricated devices[7−9] that offer unprecedented control over the size, shape, and spacing of the neural electrodes. However, neither microwire nor silicon-based devices can reliably retain a NPD−tissue interface sustaining communication with neurons over long periods of time.[10] One of the distinctive reasons for the loss of device functionality is formation of the scar from glial cells around the brain implants due to chronic inflammation.[11,12]

Initial electrode insertion inevitably damages the blood-brain barrier (BBB) by rupturing multiple blood vessels in the brain. Penetration of plasma proteins in brain tissue leads to activation of glial cells, initiation of immune response cascade,[13] and onset of scarring. Minimization of the physical "footprint" of NPDs to reduce the BBB damage is most significant at this stage.

With time, other physical characteristics of neural electrodes also contribute to inflammation that eventually becomes chronic. One could notice that there is a staggering mismatch between the mechanical properties of

* Address correspondence to kotov@umich.edu.

Received for review April 25, 2013 and accepted August 9, 2013.

Published online August 09, 2013
10.1021/nn402074y

the electrodes and tissue.[14] The Young's modulus of silicon and metals—typical materials for most NPDs for brain—spans the range from 70 to 180 GPa. The stiffness values of typical implants are about 5 orders of magnitude higher compared to the Young's modulus of the brain (1 kPa). The mechanical behavior of NPDs in soft matrix depends on the size/shape of implants, in the case when such behavior of the NPD is noncompliant with the tissue, such as when the system does not behave as a single body and there is a discontinuity of deformations at the interfaces. Such strong discrepancy of stiffness of adjacent macroscopic objects cannot remain unnoticed by the cells especially over the long period of time because many cellular functions are reactive to mechanics of the cellular environment.[15] Importantly, the stiff inflexible nature of the implants generates mechanical stress around it due to the microscale motions between the stationary implant and the soft brain tissue in the course of everyday movements of the body. These mechanical stresses caused by the mismatch in mechanical properties are essential for consideration of glial scar formation because they are believed to stimulate mechanoactivated signal transduction pathways of resident immune cells[16] and lead to chronic BBB disruption by continuous damage to surrounding blood vessels.[17] Soft and flexible neural electrodes are needed to reduce the mechanical mismatch and improve the mechanical compliance of NPDs in the brain tissue.

Besides the reduction of the initial damage and improvement of materials compliance between the material and the soft tissues, there is another reason to minimize the dimensions of NPDs. They need to be small with at least two physical dimensions comparable to that of cells (~10 μm) because crossing this threshold is expected to reduce the probability of macrophage adhesion,[18−20] while retaining the ability to form tight junctions between neurons and electrodes should still be retained.[21] Indeed, carbon fiber NPDs with diameter of ~8 μm showed marked reduction of chronic inflammation,[20] while being able to record activity of single neurons in the motor cortex of rats. Carbon fiber, however, still has a Young's modulus as high as 250 to 500 GPa and has suboptimal electrochemical parameters essential for neural implants (conductivity, impedance, charge storage capacity).

An additional aspect of NPDs related to the inflammation that needs to be addressed here is the implantation procedure. Typically, it can be described as micromanipulator-controlled surgical insertion of the device in the tissue reaching a specific depth corresponding to the desirable cell layer in the motor cortex or other part of the tissue. Notably, the implant stiffness is quite helpful for the surgical procedure and enables its facile penetration into the soft brain tissue. Hard-rod types of NPDs are being widely used, in part, for simplicity of the implantation procedure, and the realization that this format of the device may not optimal for its subsequent functionality becomes apparent only after consideration of all the issues related to micromotions and stiffness mismatch described above. On the other hand, there is no alternative up to date to this surgical protocol because of the fundamental difficulties of penetrating a soft object by an equally soft object.

Therefore, we can identify three interconnected NPD requirements for the reduction of the inflammatory reaction of the brain tissue and related improvement of their long-term functionality: (a) drastic improvement of electrode mechanical compliance with the tissue; (b) reduction of its dimensions; and (c) development of a new surgical procedure capable of implanting flexible compliant NPDs. These NPD requirements directly translate into material properties. Assuming that a device can be manufactured in some way and is nontoxic to neurons, the NPD inflammation problem can be restated in terms of materials properties as follows: we need to have the material simultaneously (a) be strong enough to enable miniaturization to dimensions <10 μm, (b) be flexible enough to be compliant with tissues at these dimensions, (c) be conductive enough in the bulk to support a sufficient amount of charge passing through it for neural recordings or stimulation, (d) form a cell−electrode interface with minimal charge transport losses (*i.e.*, with minimal impedance, Z), and (e) be tough enough to withstand a variety of deformations during some kind of implantation procedure and over the period of its operations (several years) without deterioration of electrical and other properties. According to our calculations based on a target resistance of 10 μm by 10 μm electrode (see Supporting Information), the requirement for bulk conductivity is probably the easiest one to achieve and could be satisfied by many metals. However, the other requirements represent a challenge.

Many scientists realized the need for advanced materials to improve interfacial transport and minimize impedance between cells and NPDs. This led to a tremendous amount of research effort resulting in the use of gold films,[22−24] iridium oxide (IrO_x),[25] conductive polymers,[9] carbon nanotubes (CNTs),[26] and other NPD materials. Nevertheless, these materials are utilized mostly as coatings on electrodes made from other materials because the toughness and strength of free-standing thin sheets of IrO_x and gold are not sufficient enough to withstand stresses typical for NPDs. Therefore, the most common approach for fabrication of the flexible electrodes is to combine polymer substrate with conductive coating.[22−24] However, such devices did not, so far, resolve the mechanical mismatch issue or produced composite electrodes that satisfy the aforementioned requirements, which highlights the need for the new materials for neuroprosthetic

devices. Their availability will help to avoid harsh compromises between the device functionality, its size, and the inflammatory side effect limiting the longevity.[27,28]

A special analysis needs to be given to CNT-based NPDs because there has been an overwhelming number of studies demonstrating that CNTs have exceptional material properties for neural interfaces[29] in terms of electrochemical performance,[30] chemical stability,[31] and mechanical properties.[32] Surveying the state-of-the-art of NPDs from CNTs, we can see again how difficult it is to satisfy the materials requirements (a−e) discussed above and combine desirable mechanical and electrical properties. Typically, CNT layers were made on polymer substrates by using low-temperature growth conditions[33] as well as stamping techniques.[34,35] These methods often give rise to weak adhesion between CNTs and substrates. Consequently, buckling behavior during device implantation led to delamination and device failure.[36] Thus, electrodes with only relatively large dimension of 200 μm in width have been fabricated by these techniques.[34] Layer-by-layer (LBL)-assembled CNTs can improve adhesion, strength,[32] flexibility, conductivity,[37,38] and impedance[30] of the conductive films. Several *in vitro* studies reported successful neuron/neural stem cell cultures and direct neural stimulation/recording on LBL-made CNT substrates.[26,39−44] *In vivo* studies with CNT-modified traditional electrodes showed that the CNT coatings enhanced the recording quality of NPDs[45] and improved the chemical stability of the recording materials.[31] Similarly to noble metals and IrO_x, all of these studies describe the use of CNT *coatings* on traditional metal electrodes or on silicon substrates. A recent publication describes CNT-based fibers made by dielectrophoretic assembly.[46] This work can be an interesting example of a free-standing CNT electrode, but at the same time, these electrodes were implanted using standard hard-rod penetration technique and neural recordings were similar in quality to free-standing carbon fiber electrode.[20] The problems with the mismatch of mechanical properties, realization of the tissue-compliant devices, their miniaturization, development of a new surgical procedure for their implantation, and finding out the corresponding effects on long-term scarring, therefore persist.

In this study, we aimed to demonstrate the fundamental possibility of flexible tissue-compliant devices with at least two dimensions comparable to those of cells, namely, thickness and width of the flexible strips. Since this goal led to necessary departure from the standard NPD protocols, we also searched for new methods to manufacture flexible substrate-less electrodes and their implantation in the brain tissue. We took advantage of mechanical and electrical properties of LBL-made CNT nanocomposites and manufactured flexible and compliant NPD devices. Their successful insertion in the motor cortex area could be visualized by two complementary imaging techniques, while their functionality was verified by registration of brain activity in this area in the form of low-frequency neural recording.

RESULTS AND DISCUSSION

As a materials foundation of this project, we decided to take LBL-assembled CNT composites that represented themselves well in the form of coatings[26,30] and in various tests for materials properties.[32,38] Their toxicological profile,[47] strength, flexibility, conductivity, impedance, and toughness were demonstrated to be adequate to satisfy requirements (a−e) outlined above. Although we do not know enough about their long-term stability in tissues and biological effects on adjacent neuronal and other cells, these materials can be a promising starting point for this study. In this case, the first challenge on the way to small tissue-compliant LBL-made nanocomposite electrodes is the development of microfabrication techniques adequate for miniature NPDs with dimensions of ~10 μm.

Microfabrication. We decided to address this challenge by integration of the layered CNT nanocomposites with established microfabrication technologies that are similar to those used in MEMS devices from silicon. The composite neural electrodes were fabricated using a two-mask process with an optical photolithography technique illustrated in Figure 1A. The CNT nanocomposite was LBL-assembled from nanotubes wrapped with poly(sodium 4-styrenesulfonate) (PSS) and poly(vinyl alcohol) (PVA) as partner polymers following the process described in our previous publications.[30,32] As a substrate, we used glass coated with parylene-C by chemical vapor deposition (CVD). Note that the versatility of LBL assembly and its ability to form strongly adhesive layers even on such an unlikely underlying material as hydrophobic parylene-C plays a significant role in the realization of this protocol. Equally important is the fact that a photoresist can be uniformly spun on the LBL-made CNT composites. Both of these seemingly mundane attributes of the well-known process enable a wide spectrum of micromanufactured architectures and devices made from composite materials.

After developing the photoresist, the LBL-made CNT composite and the first parylene-C layer were etched by oxygen plasma. Compared to the manufacturing protocols for fabricating metal/polymer flexible electrodes used previously,[48] this method eliminated the extraneous steps of lift-off and wet etch of metal that could introduce additional toxic components in the composite. The second layer of parylene-C was deposited after the plasma etching to serve as the top insulation layer for the neural probe. The entire substrate was etched slowly by oxygen plasma to avoid erosion of the CNT composite. This slow etching step served the purpose to expose the parylene-covered

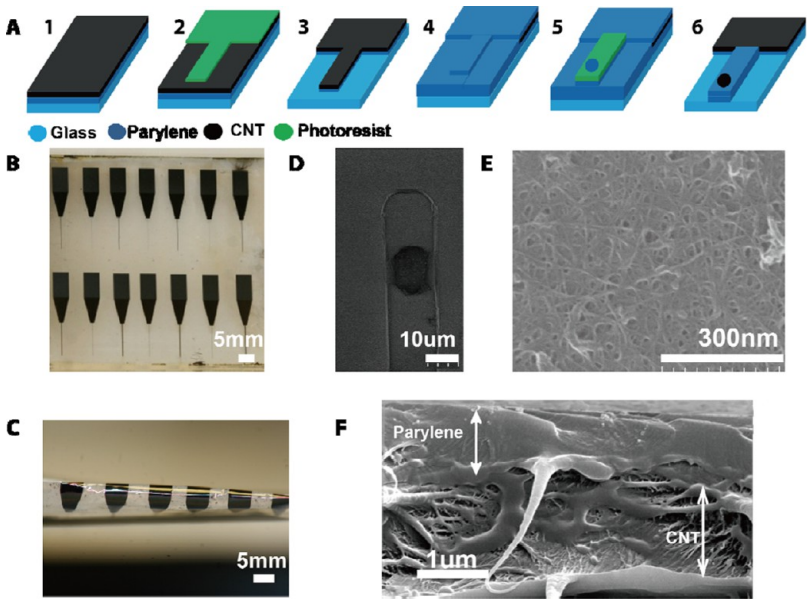

Figure 1. (A) Fabrication scheme of the nanocomposite electrodes combining LBL and MEMS-like microfabrication. (B) Optical image of composite electrodes on glass substrate. (C) Nanocomposite electrode on parylene-C sheet bent at 180° to demonstrate flexibility. (D) SEM image of a composite electrode with a width of 10 μm. The "window" in the parylene-C coating serves as the neural recording site and has high contrast with the insulating coating due to electrical conductivity of the LBL-made CNT composite. (E) Close-up SEM image of the CNT neural recording site on the 10 μm wide electrode. (F) Cross-section SEM image of the recording site on the fabricated electrodes. Distortion of the parylene-C and composite layers of the device occurs due to sheer stress due to cutting. Note that no delamination of the CNT composite layer can be observed.

CNT composite as the recording site. The electrodes were fabricated on the glass substrate and were lifted-off with HF to produce free-standing devices after wire bonding to the circuit lead. Note that HF is highly toxic to all cells and volatile. Within the limits of the current knowledge, it does not affect the biocompatibility of the nanocomposite devices because it can be easily removed by washing. Care needs to be given though to this step and avoid potential problems related to its toxicity. Other lift-off techniques can also be utilized for LBL films that do not involve HF.[60]

The implantable part of the nanocomposite electrode had a thickness of 3 μm along the shaft and 2 μm at the recording site (Figure 1F and Figure 3G). These NPD dimensions are smaller than typical cell diameters and within the dimensional targets set for this project. Micrometer-scale thickness provided the electrodes with required flexibility. Deformations that might be considered to be extreme for NPD devices (Figure 1C) do not affect its integrity due to high strength and adhesion of the CNT composite to parylene-C. The nanocomposite electrode can be flexed over 180° without breaking.

The width of the electrode is the second dimension that would be desirable to reduce to sizes comparable to that of neurons. Here we varied the width of the electrodes in three sizes: 10, 25, and 50 μm. The smaller versions of the composite NPDs are within the desirable size range and dimensional targets for NPD width. They are equal or comparable to the smallest implantable electrodes reported so far.[20,42,46] Our electrodes are also considerably smaller than other silicon-based devices.[8,9] The high strength of the LBL composites without high bending stiffness will facilitate their further miniaturization.

The recording sites were varied between three different sizes: ~100, ~625, and ~2500 μm^2 depending on the width of the implant. The examination of the micromanufactured NPDs by scanning electron microscopy (SEM, Figure 1D) showed that the 100 μm^2 recording site at the tip of the electrode was highly conductive while the rest of the composite electrode was insulated by parylene-C. A zoomed-in image of the recording site showed that the integrity of the CNT composite is preserved through the fabrication process (Figure 1E).

The total length of the shaft of the micromanufactured electrode was 5000 μm (Figure 1B), which is sufficient to reach deep structures within the rat and human brain. For comparison, the depth of the motor cortex in rats is 5000 μm,[49] while the same for humans is 20 000 μm.[49] Depending on the clinical purposes of neural recording, the smaller depths of implantation could be targeted and even preferred, as well.

Mechanical Properties. After successful fabrication of the electrodes, mechanical tests were performed to better understand the mechanical properties of the micromanufactured neural electrode (Figure 2A). The complete analysis will require detailed finite element modeling of the system consisting of hard beam with rectangular or cylindrical cross-section in a soft matrix for different deformations as well as for vibrations, which should be the subject of a separate study.

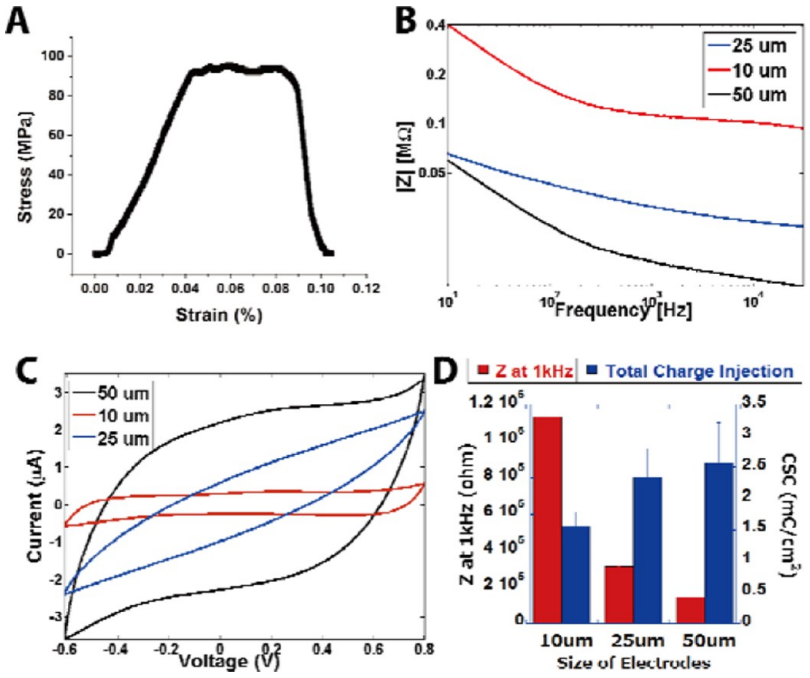

Figure 2. (A) Tensile test of nanocomposite electrode, Young's modulus of 2.2 GPa. (B) Typical impedance (*Z*) of the electrodes with different sizes of the functional sites. (B) Typical cyclic voltammetry of the electrodes with different sizes of the functional sites, sweep from 0.8 V to −0.6 V at 1 V/s scan rate. (C) Cumulative electrochemical properties of the nanocomposite electrodes. Eight electrodes were tested for each size.

Here we suggest a simplified version of evaluation of mechanical compliance based on the mechanical damage to the tissues upon deformations to the implant that is reflective of the chronic BBB trauma around implants. In this approximation, we describe mechanical compliance with brain tissue by comparing the pressure associated with buckling deformation of the implant and the critical rupture strength of the brain tissue. If the pressure from the brain to buckle the implant is higher than the critical rupture strength of the brain tissue, this system will be considered to be noncompliant and *vice versa*.

Buckling force for a simple beam is a function of geometry and Young's modulus. The specific expression for calculating the buckling force of a rectangular beam is given by eq 1.

$$F = \frac{\pi^2 EI}{(KL)^2} \quad (1)$$

where E is the Young's modulus, which is 2.2 GPa for the nanocomposite electrode (Figure 2A); I is the area moment of inertia; L is the unsupported length of the beam; and K is the column effective length factor, which is 0.5 for the two-end fixed beam. We can consider that the nanocomposite electrode is a rectangular cross-sectional beam with dimensions of 5000 μm in length, 3 μm in height, and 10 μm in width. For this geometry, the area moment of inertia is

$$I = \frac{h^3 w}{12} \quad (2)$$

where h is the height and w is the width. We can calculate the force required for the electrode to buckle and convert this force to a pressure term by considering the footprint of the electrodes. This pressure is about 2.37 kPa for the nanocomposite electrode. It is smaller than the critical rupture strength of the brain tissue, which is typically about 3 kPa.[50] This indicated that the composite electrode will likely deform before inducing the brain tissue rupture.

Electrical Properties. We evaluated their electrochemical performance in terms of impedance (Z) and charge storage capacity (CSC) measured in a three-electrode electrochemical setup and calculated with a custom MATLAB (Mathworks Inc., MA) script. The exact Z and CSC needed for NPDs depend on neural tissues and the type of the projected treatment/interface.[27] Nevertheless, the minimization of Z and maximization of CSC are the typical requirements for implantable electrodes as they reflect the key electrochemical parameters for their reduction of noise in NPDs, reduction of electrical damage to the tissue, and improving their long-term performance. Impedance was measured by a frequency response analyzer from 10 Hz to 32 kHz for three different sizes of electrodes (Figure 2B). As expected, we observed a negative correlation between electrode size and impedance since larger electrodes have higher electrical conductance and larger surface area for the functional site. The impedance decreased as the voltage frequency increased which was also expected from the resistor/capacitor model for impedance[51] because Z is inversely related to frequency. Capacitive response dominates the impedance values at high

frequencies. Importantly, we found that the impedance of the 10 μm wide electrode with 100 μm^2 site is ~1 MOhm at 1 kHz, which is the physiological relevant spiking frequency of neurons. $Z = 1-2$ MOhm is considered to be sufficiently low to allow for successful recordings of neural activity.[27,59] These data also indicate that future development of the NPD materials will need to address further reductions of the impedance because we would want to miniaturize the electrode even more. This goal will necessitate further improvements in conductivity of the material and its interface with tissues. The recently developed highly conductive composites based on gold nanoparticles could be potential candidates.[61]

Cyclic voltammetry (CV) curves obtained at a scan rate of 1 V/s from −0.6 to 0.8 V (Figure 2C) were used to calculate CSC. For quantitative comparison among electrodes of different sizes, we plotted the impedance magnitude of the electrodes at 1 kHz and the total amount of charge injected by integrating the area enclosed in the CV curve, which is a key parameter for neural stimulation (Figure 2D). The correlation between electrode size and electrochemical properties indicated the precision over the control of the electrode's functional site. We obtained a CSC value of 1.55(±0.34) mC/cm^2 for 100 μm^2 recording site and 2.57(±0.76) mC/cm^2 for 2500 μm^2 recording sites (Figure 2D).

Surgical Procedure. As expected, the softness and flexibility of the nanocomposite electrodes became a major challenge during the electrode insertion into the brain. Several methods were considered to circumvent the problem of insertion of a soft ribbon into soft matrix, such as using water-soluble polymers to temporarily stiffen the probes[52] and chemically modified probe-releasing shuttles.[53] The use of stiffening materials was not favored by us because (a) they inherently restrict the size of the implant to those that can perform as stiff rods, which limits the possibilities of microminiaturization (b) remnants of the polymers can cause inflammation; and (c) if products of biodegradation of such polymers remain at the NPD−tissue interface, they will increase interfacial impedance.

To have a more universal technique to implant soft electrodes, we tested the use of an electrode-releasing shuttle, taking advantage of capillary interactions between the composite strip and a simple gold wire (60 μm in diameter, A-M Systems). The gold wire was used as received and was not modified or micromanufactured in any way except antiseptic treatment. A completed description of the procedure of the electrode's insertion is given in Supporting Information Figure S2. In brief, the flexible micromanufactured electrode and the metal wire were initially stored in dry ice for more than 1 h. Then the electrode and the needle were removed from the dry ice and kept at room temperature until water condensed on both objects. The composite electrode was placed on top of the wire adhering to it *via* condensed water. The entire assembly was stored in a refrigerator at −20 °C until the implantation. After the craniotomy on the animal was performed, the electrode-on-the-needle assembly was removed from the refrigerator, transferred in dry ice to the surgical table, and quickly inserted into the brain tissue by a micromanipulator. When the interfacial ice layer between the shuttle and electrode melted, the shuttle was removed while the flexible electrode remained inside the brain. This method allowed us to insert the produced flexible electrodes without any additional chemicals of polymeric or other nature. We believe it can also be equally applicable to other tissue-compliant NPDs because the capillary forces are generic and temporary attachment of the flexible strips to the gold needle can also be accomplished for other materials. The initial footprint of the shuttle can be further miniaturized by selecting/manufacturing smaller and thinner needles that can be potentially as thin as nanowires.

Post-Surgery Imaging. To assess the integrity of the electrode after the implantation and its resilience to shear forces during the surgery, we removed the electrode from the brain and investigated the cross section of the implanted electrode by SEM (Figure 3G). As one can see, the structure of the device was well-preserved and no obvious delamination of neither the top nor the bottom layer of the electrode occurred.

Several aspects of implantation method need further evaluation for its routine usage, such as the effect of the initial low-temperature condition to the brain, sterile condition of the ambient condensed water, and initial acute damage from the shuttle. Here we made a preliminary investigation of the tissue damage induced by the procedure using *ex vivo* confocal microscopy. The electrode was green stained with FITC-albumin solution prior to implantation (Figure 3F); the brain tissue cells were stained with toluidine blue having red luminescence after electrode implantation. We observed a concentration of brain cells close to the electrode (bright red emission). The size of this particular area is similar to the shuttle footprint (50 μm). It is possibly because the shuttle insertion damaged the extracellular matrix and packed brain cells close together. Alternatively, the same imaging effect could be associated with the cellular damage that is reflected by the higher permeability of the dye. The effect of this damage on the long-term functionality of the CNT electrodes and its relationship to chronic inflammation will require further study.

In addition to trauma assessment, noninvasive and label-free imaging techniques are important to guide/monitor the electrode through different stages of the implantation.[54,55] In this study, the state of the electrodes after implantation was examined by two imaging

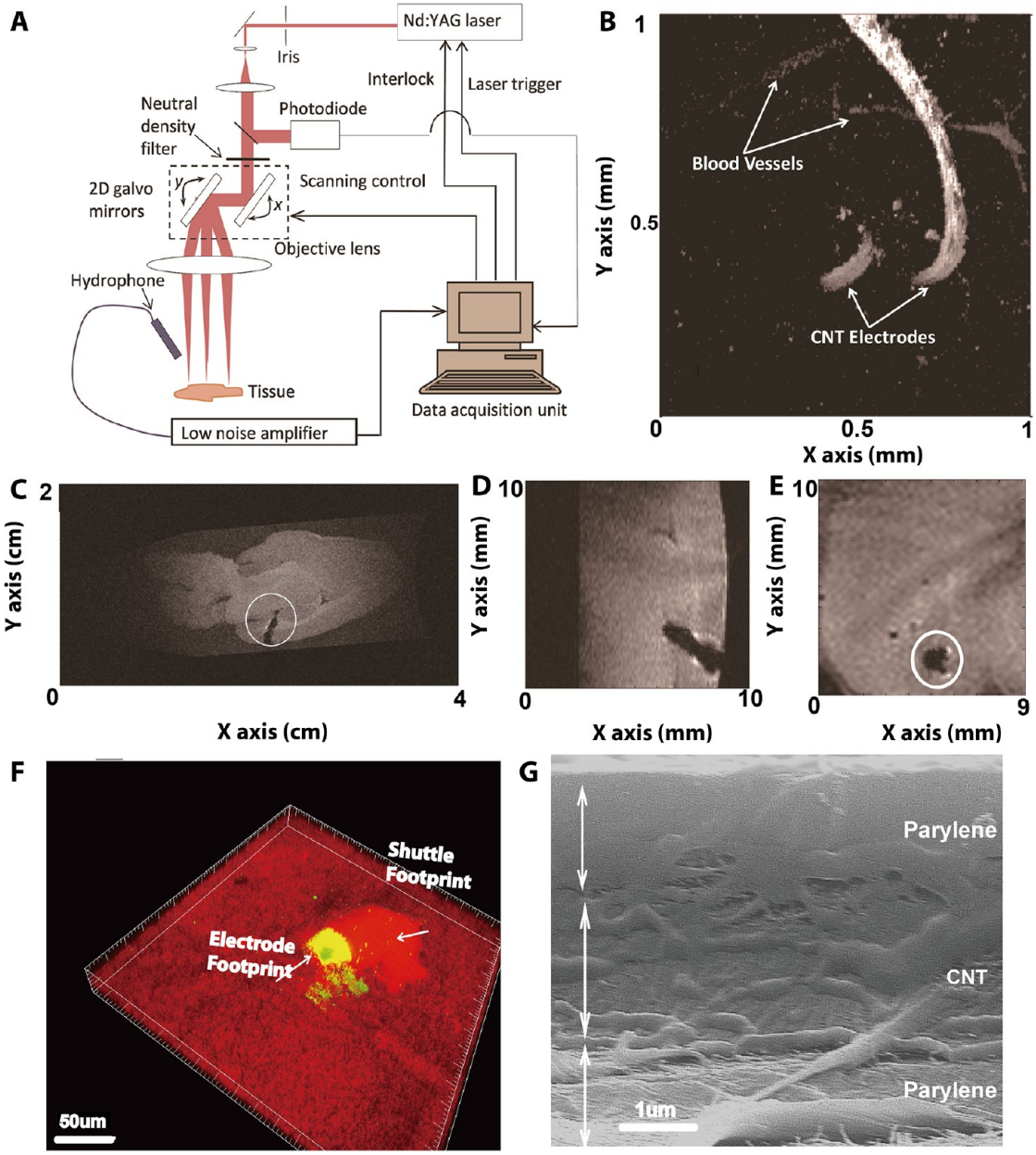

Figure 3. (A) Schematic of the photoacoustic microscopy (PAM) setup. (B) PAM image of two electrodes inserted into the brain. (C) MRI image of the implant in the *y*−*z* plane (Sagittal plane). (D) Zoomed-in MRI image of the *y*−*z* plane (Sagittal plane). (E) MRI image of the *x*−*y* plane (transverse plane). (F) Confocal microscopy of brain tissue and inserted electrode. Electrode was stained with FITC (green), and cells were stained with toluidine blue (red). (G) Cross-section SEM image of the electrode after brain insertion. There are three distinct layers as labeled in the graph.

modalities *ex vivo*: photoacoustic microscopy (PAM)[56,57] and magnetic resonance imaging (MRI).

Prior to electrode insertion and after craniotomy, one needs to closely assess the insertion site to identify the specific region of interest and also avoid blood vessels to minimize bleeding and BBB trauma. PAM combines optical and acoustic imaging techniques to produce images with excellent optical contrast and great imaging depth. This technique is based on the difference of optical absorption in tissues and was realized by rastering laser beam over the brain tissue (Figure 3A). It offers higher imaging depth than optical microscopy and provides the same functional information. It would be an excellent tool for monitoring vasculature within the region of the interest that could potentially compete with two-photon microscopy (TPM).[54,55] In our specific setup, photoacoustic signals were detected by a calibrated needle hydrophone and the ultrasound coupling was through water. With this imaging system, we can achieve lateral resolution of 5 μm and axial resolution of 100 μm. Figure 3B represents a surface PAM image of the nanocomposite electrode inserted into the brain tissue. Due to its strong optical absorption, the nanocomposite

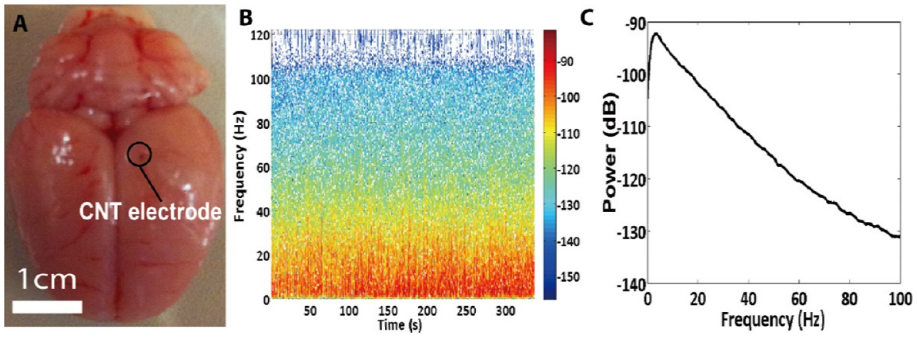

Figure 4. (A) Harvested animal brain after recording experiment. (B) Low-frequency signal recorded from the brain with the 10 μm wide nanocomposite electrode (100 μm^2 recording site). (C) Power spectrum of the low-frequency signal recording; signal peak at 5 Hz.

electrodes displayed high contrast in the image, which is the portion of the electrode outside of the brain in Figure 3B. CNT electrodes were curved from the side due to its flexibility, and we purposefully curved the particular part of the electrode to observe where the electrode was inserted. Moreover, we could also visualize the vasculature near the brain surface due to strong absorption of hemoglobin. Three-dimensional mapping of the blood vessels is very important for electrode insertion.[54,55] PAM makes possible high-resolution imaging of blood vessels in the brain tissue which can be utilized to minimize their rupture during the insertion procedure, thus reducing insertion trauma and preserving brain cells from contact with blood components resulting in inflammation reactions. Combining electrodes with high PAM contrast image of blood vessels could be a valuable tool for clinical neural surgery.

Assessing implanted flexible neural electrodes inside the brain during and after the surgery is also crucial, especially after the electrodes were closely sealed inside the skull. MRI is a well-established technique that can provide a noninvasive and high-depth 3D image of the nanocomposite electrodes inside the brain.[58] It could monitor precisely the position of the electrode with the skull intact. We acquired MRI images after implanting the compliant electrode from nanotubes (Figure 3C–E). The high contrast of the nanocomposite electrode is attributed to both the loss of water proton and disturbance of the magnetic field created by the nanocomposite electrodes. Figure 3C is the cross-sectional view of the electrodes in the brain. We observed that the implant procedure successfully delivered the electrode into the brain without any kinks or curvature, which is essential for both accuracy of its placement in motor cortex and mechanical deformation behavior. Figure 3E is the zoomed-out image of the cross-sectional view. We can identify the position of the electrode and the depth of the electrode in the brain to be 500 μm, which is the forelimb control area of the primary motor cortex in rats.

Recording of Brain Activity. After verifying the electrochemical performance of the as-fabricated neural electrodes and carefully assessing the state of the neural electrodes, we conducted *in vivo* physiological recording experiments with rats. The typical procedure of the animal preparation and neural recording was published previously[9] and is described in the Materials and Methods section. The neural electrode with 100 μm^2 recoding site was inserted into the brain tissue as described in the previous paragraph. Nanotube electrodes were inserted into four different animals. Acute neural recordings were conducted immediately after electrode insertion. Figure 4C is the typical low-frequency neural signal recorded over time. The color spectrum of the plot represents the intensity of the local field potential. We observed high signal intensity (dark red color) in the low-frequency range (0 to 20 Hz) over the entire recording session. We concluded that the electrode can record a low-frequency signal consistently over time. To further identify the peak of the low-frequency neural recording, we accumulated the intensity data over time to generate a power spectrum. The power spectrum showed a peak around 5 Hz. We did not observe any intensity peak at 60 Hz, which is common for instrumental background noise. The power spectrum clearly demonstrated that the neural electrode could specifically identify the low-frequency neural signal from instrumental noise (Figure 4D). Furthermore, we conducted a blank recoding experiment in buffer saline solution. We observed much lower signal power compared to the recoding in the animal brain (Supporting Information). We did not observe single neural spike in our recording session; it is possibly due to the effect of isoflurane as anesthetic agent.[59] Electrical problems with interfacial contact of brain cells are also possible, although less likely, and will be carefully evaluated continuing this work.

CONCLUSIONS

This study demonstrated that LBL assembly is capable of producing tissue-compliant CNT nanocomposites

with electrochemical performance particularly suitable for neuroprosthetic devices. These composites can be microfabricated with required precision using standard photolithography technology into flexible neural electrodes. The footprint of the electrodes can be miniaturized to 10 μm in width with thicknesses as small as 3 μm, which is smaller than any stiff[18] or flexible[38] functional NPDs reported to date. Importantly, the process of implantation of such compliant devices was developed, which could be applied to other devices with similar mechanical properties made from nanocomposites or other suitable materials satisfying conditions discussed above. We want to point out that better understanding of the mechanics of the flexible brain implants in soft brain tissue and, therefore, requirements for the materials used in neuroprosthetic devices is needed.

The low-frequency neural signal was recorded in the animal model to demonstrate the functionality of the neural electrodes. Further exploration of high-frequency recordings of neuronal signals and microfabrication of arrays of tissue-compliant electrodes is necessary. If the ability to record high-frequency signals and single neuronal activity requires changes in electrode design in addition to the use of a different anesthesia drug, the developed MEMS-like manufacturing process that we used for these electrodes provides such capabilities as well as the potential for further miniaturization. Similarly to our previous study,[20] the evaluation of the chronic tissue response should also be carried out to demonstrate the long-term functionality and inflammation response of this new class of nanocomposite electrodes. We also utilized both emerging and well-established imaging modalities to examine these flexible neural electrodes in the brain. In aggregate, the results reported in this paper take us a step further to the use of nanocomposite-based neural prosthetics in a clinical setting.

MATERIALS AND METHODS

High-purity single-wall carbon nanotubes (P2-SWNTs, >90% purity) were purchased from Carbon Solution, Inc. (Riverside, CA). Poly(vinyl alcohol) (PVA; MW 70k fully hydrolyzed) and poly(sodium 4-styrenesulfonate) (PSS; MW 100k) were obtained from Sigma-Aldrich. All other chemicals were obtained from Sigma-Aldrich.

Layer-by-Layer Assembly of SWNT Film was initially carried out on microscope glass slides cleaned in piranha solution (mixture of sulfuric acid and hydrogen peroxide DANGEROUS!) overnight and then thoroughly rinsed with deionized water prior to the use. SWNTs were first dispersed at 0.5 mg/mL in 2 mg/mL PSS (MW 100k) solution by ultrasonication. A 0.1 wt % PVA solution was prepared by dissolving the correct amount of PVA in near boiling water. For each deposition cycle, the electrode was immersed in the PVA solution for 2 min, followed by rinsing with deionized water and drying with an air stream. Then the electrode was immersed in SWNT solution for 5 min, followed by rinsing with deionized water and drying with an air jet. The cycle was repeated 300 times by a commercially available LBL deposition robot (NanoStrata Inc., Tallahassee, FL).

Electrode Fabrication. First, 800 nm parylene-C thin film was deposited by chemical vapor deposition method (PDS 20350, SCS Equipment) on a clean glass slide. The first layer of parylene-C served as the bottom insulation layer for the electrodes. Then a 1 μm CNT:PSS/PVA nanocomposite was deposited on the parylene-C film using the layer-by-layer (LBL) assembly method. After parylene-C and CNT composite deposition, the positive photoresist (SPR220-3.0, Rohm Haas) was spin coated and exposed by the first mask on the CNT composite. After developing the photoresist, the entire substrate was treated by oxygen plasma (790 RIE, Plasma Therm) to pattern the base layer of the neural electrodes. After the oxygen plasma etching, a second layer of parylene-C was deposited onto the base layer. This served as the top insulation layer for the neural probe. Then the positive photoresist was spin coated again and exposed by the second mask on top of the second layer of parylene-C. The entire substrate was etched slowly by oxygen plasma to avoid overetch of the CNT composite. The second mask created the outline for the final electrode shape and opened the functional CNT site at the tip of the electrodes.

Scanning Electron Microscopy (SEM) images were obtained using a FEI Nova Nanolab SEM at 10 kV accelerating voltage.

Electrochemical Impedance Spectroscopy (EIS) was carried out on an Autolab PGSTAT 12; Frequency Response Analyzer software (EcoChemie, Utrecht, Netherlands) was used to record impedance spectra of the electrodes. A solution of 1× phosphate buffered saline (PBS, pH = 7) was used as an electrolyte in a three-electrode configuration. The working electrode was connected to the electrode site. The counter electrode was connected to a gold foil immersed in PBS, and a Ag/AgCl reference electrode was immersed in PBS. An AC sinusoidal signal of 25 mV in amplitude was used to record the impedance over a frequency range of 10−32000 Hz.

Cyclic Voltammetry (CV) experiments were performed using an Autolab PGSTAT 12 instrument and General Purpose Electrochemical System software (EcoChemie, Utrecht, The Netherlands) in a three-electrode configuration as described for EIS. For CV, a scan rate of 1 V/s was used and the potential on the working electrode was swept between −0.8 and 0.6 V. Three cycles were swept to ensure that the film had reached a stable state.

Craniotomy Preparation. Adult male 550−600 g Sprague−Dawley rats (Charles River Laboratories) were anesthetized with 2% isoflurane. The depth of anesthesia was observed by monitoring heart rate and breathing rate. The animal was placed into a stereotaxic frame, and a 2 mm by 2 mm craniotomy was made over the motor cortex. Once the dura was incised and resected, the animal brain was ready for implantation.

***In Vivo* Electrophysiological Data** were recorded using a TDT RX5 Pentusa Recording System (Tucker-Davis Technologies, Alachua, FL). These neuronal signals were acquired through a head-stage buffer amplifier to avoid signal loss in data transmission. Signals were sequentially filtered by an anti-aliasing filter in the preamplifier, digitized at a ∼25 kHz sampling rate, and digitally band-pass-filtered from 2 to 5000 Hz. Wideband signals were acquired to capture both spiking and local field potential (LFP) activity. Signals were continuously recorded in 10 min intervals. Neural recording segments were analyzed offline using a custom automated MATLAB (Mathworks Inc., MA) script. LFP power spectral density plots were created using a Hamming window for smoothing with a 32768 point fast Fourier transform (FFT).

Photoacoustic Microscopy was carried out through a Nd:YAG laser (Spot-10-200-532, Elforlight Ltd., UK) working at 532 nm with a pulse duration of 2 ns and a repetition rate (PRR) of 0−50 kHz. The laser light was spatially filtered by an iris and then expanded to a parallel beam which was rastered over the tissue object by 2D galvanometers. The intensity and the stability of the laser beam was monitored and calibrated by a

photodiode (DET10A, Thorlabs, NJ). An achromatic lens with a focal length of 50 mm was used as the objective lens. Photoacoustic signals were detected by a calibrated needle hydrophone (HNC-1500, Onda, CA) with −10 dB bandwidth of 300 kHz to 20 MHz. The distance between the hydrophone and the tissue was 5 mm, and the ultrasound coupling was through water. The detected photoacoustic signals, after a low noise amplifier (AH 2010, Onda, CA), was digitized by an A/D card (Razor CS14X2, GaGe, IL). The spatial resolution of this system was measured by imaging a USAF resolution template (T-20-P-TM, Applied Image Inc., NY). The lateral resolution was 5 μm, determined by the optical focusing. The axial resolution of this system was 105 μm, which was limited by the central frequency and bandwidth of the hydrophone.

Magnetic Resonance Imaging was performed with a 3D gradient echo pulse sequence at 2.0 T (Varian Inc., Palo Alto, CA) using a home-built RF coil. Data were obtained with TR = 100 ms and TE = 10 ms and with 100 μm isotropic voxels. Following acquisition, the data were processed by scripts written in MATLAB (The Mathworks, Natick, MA).

Confocal Microscopy was performed by a commercial Leica Inverted microscope. The nanocomposite electrode was stained by soaking in FITC-albumin solution (1 mg/mL) for 1 h. The brain tissue was stained by toluidine blue for an hour (5 mL of 0.01 mg/mL ethanol solution diluted in 45 mL of 1% sodium chloride solution).

Conflict of Interest: The authors declare no competing financial interest.

Acknowledgment. We acknowledge support from NSF under Grants ECS-0601345, EFRI-BSBA 0938019, CBET 0933384, CBET 0932823, and CBET 1036672. The work is also partially supported by AFOSR MURI 444286-P061716 and NIH 1R21CA121841-01A2. This material is based upon work partially supported by the Center for Solar and Thermal Energy Conversion, an Energy Frontier Research Center funded by the U.S. Department of Energy, Office of Science, Office of Basic Energy Sciences under Award No. DE-SC0000957. Z.X. is grateful to Samsung GRO 2012 Program and NSF Grant No. DBI-1256001 for partial support in the course of this project. The authors thank the University of Michigan's EMAL for its assistance with electron microscopy and for the NSF Grant No. DMR-9871177; Dr. Takashi D. Yoshida Kozai (Biomedical Engineering, University of Pittsburgh), Prof. Cindy Chestek (Biomedical Engineering, UM), Prof. Daryl R. Kipke (Biomedical Engineering, UM), and Prof. Euisik Yoon (Electrical and Computer Engineering, UM) for assistance and helpful discussion on electrochemical methods and neural electrodes; Terry Shyu and Jian Zhu for helpful discussion on mechanical properties of the materials; and Sahar Rahmani for assistance on confocal microscopy. This work was partially performed in the Lurie Nanofabrication Facility (LNF).

Supporting Information Available: Additional figures and experimental details. This material is available free of charge *via* the Internet at http://pubs.acs.org.

REFERENCES AND NOTES

1. Kennedy, P. R.; Bakay, R. A. Restoration of Neural Output from a Paralyzed Patient by a Direct Brain Connection. *NeuroReport* **1998**, *9*, 1707–1711.
2. Donoghue, J. P. Connecting Cortex to Machines: Recent Advances in Brain Interfaces. *Nat. Neurosci.* **2002**, *5*, 1085–1088.
3. Callaghan, J. C. Early Experiences in the Study and Development of an Artificial Electrical Pacemaker for Standstill of the Heart: View from 1949. *Pacing Clin. Electrophysiol.* **1980**, *3*, 618–619.
4. Hochberg, L. R.; Serruya, M. D.; Friehs, G. M.; Mukand, J. A.; Saleh, M.; Caplan, A. H.; Branner, A.; Chen, D.; Penn, R. D.; Donoghue, J. P. Neuronal Ensemble Control of Prosthetic Devices by a Human with Tetraplegia. *Nature* **2006**, *442*, 164–171.
5. Strumwasser, F. 'Long-Term Recording' from Single Neurons in Brain of Unrestrained Mammals. *Science* **1958**, *127*, 469–470.
6. Ellis, T. L.; Stevens, A. Deep Brain Stimulation for Medically Refractory Epilepsy. *Neurosurg. Focus* **2008**, *25*, E11.
7. Rousche, P. J.; Normann, R. A. Chronic Recording Capability of the Utah Intracortical Electrode Array in Cat Sensory Cortex. *J. Neurosci. Methods* **1998**, *82*, 1–15.
8. Campbell, P. K.; Jones, K. E.; Huber, R. J.; Horch, K. W.; Normann, R. A. A Silicon-Based, Three-Dimensional Neural Interface: Manufacturing Processes for an Intracortical Electrode Array. *IEEE Trans. Biomed. Eng.* **1991**, *38*, 758–768.
9. Ludwig, K. A.; Uram, J. D.; Yang, J.; Martin, D. C.; Kipke, D. R. Chronic Neural Recordings Using Silicon Microelectrode Arrays Electrochemically Deposited with a Poly(3,4-ethylenedioxythiophene) (PEDOT) Film. *J. Neural. Eng.* **2006**, *3*, 59–70.
10. Ward, M. P.; Rajdev, P.; Ellison, C.; Irazoqui, P. P. Toward a Comparison of Microelectrodes for Acute and Chronic Recordings. *Brain Res.* **2009**, *1282*, 183–200.
11. Biran, R.; Martin, D. C.; Tresco, P. A. Neuronal Cell Loss Accompanies the Brain Tissue Response to Chronically Implanted Silicon Microelectrode Arrays. *Exp. Neurol.* **2005**, *195*, 115–126.
12. Edell, D. J.; Toi, V. V.; McNeil, V. M.; Clark, L. D. Factors Influencing the Biocompatibility of Insertable Silicon Microshafts in Cerebral Cortex. *IEEE Trans. Biomed. Eng.* **1992**, *39*, 635–643.
13. Fawcett, J. W.; Asher, R. A. The Glial Scar and Central Nervous System Repair. *Brain Res. Bull.* **1999**, *49*, 377–391.
14. Subbaroyan, J.; Martin, D. C.; Kipke, D. R. A Finite-Element Model of the Mechanical Effects of Implantable Microelectrodes in the Cerebral Cortex. *J. Neural. Eng.* **2005**, *2*, 103–113.
15. Discher, D. E.; Janmey, P.; Wang, Y.-l. Tissue Cells Feel and Respond to the Stiffness of Their Substrate. *Science* **2005**, *310*, 1139–1143.
16. Keohan, F.; Wei, X. F.; Wongsarnpigoon, A.; Lazaro, E.; Darga, J. E.; Grill, W. M. Fabrication and Evaluation of Conductive Elastomer Electrodes for Neural Stimulation. *J. Biomater. Sci., Polym. Ed.* **2007**, *18*, 1057–1073.
17. Seymour, J. P.; Kipke, D. R. Neural Probe Design for Reduced Tissue Encapsulation in CNS. *Biomaterials* **2007**, *28*, 3594–3607.
18. Kim, Y. T.; Hitchcock, R. W.; Bridge, M. J.; Tresco, P. A. Chronic Response of Adult Rat Brain Tissue to Implants Anchored to the Skull. *Biomaterials* **2004**, *25*, 2229–2237.
19. Sanders, J. E.; Stiles, C. E.; Hayes, C. L. Tissue Response to Single-Polymer Fibers of Varying Diameters: Evaluation of Fibrous Encapsulation and Macrophage Density. *J. Biomed. Mater. Res.* **2000**, *52*, 231–237.
20. Kozai, T. D.; Langhals, N. B.; Patel, P. R.; Deng, X.; Zhang, H.; Smith, K. L.; Lahann, J.; Kotov, N. A.; Kipke, D. R. Ultrasmall Implantable Composite Microelectrodes with Bioactive Surfaces for Chronic Neural Interfaces. *Nat. Mater.* **2012**, *11*, 1065–1073.
21. Hai, A.; Shappir, J.; Spira, M. E. In-Cell Recordings by Extracellular Microelectrodes. *Nat. Methods* **2010**, *7*, 200–202.
22. Rousche, P. J.; Pellinen, D. S.; Pivin, D. P., Jr.; Williams, J. C.; Vetter, R. J.; Kipke, D. R. Flexible Polyimide-Based Intracortical Electrode Arrays with Bioactive Capability. *IEEE Trans. Biomed. Eng.* **2001**, *48*, 361–371.
23. Seo, J.-M.; Kim, S. J.; Chung, H.; Kim, E. T.; Yu, H. G.; Yu, Y. S. Biocompatibility of Polyimide Microelectrode Array for Retinal Stimulation. *Mater. Sci. Eng., C* **2004**, *C24*, 185–189.
24. Boppart, S. A.; Wheeler, B. C.; Wallace, C. S. A Flexible Perforated Microelectrode Array for Extended Neural Recordings. *IEEE Trans. Biomed. Eng.* **1992**, *39*, 37–42.
25. Cogan, S. F.; Ehrlich, J.; Plante, T. D.; Van Wagenen, R. Penetrating Microelectrode Arrays with Low-Impedance Sputtered Iridium Oxide Electrode Coatings. *Proc. IEEE* **2009**, 7147–7150.
26. Gheith, M. K.; Pappas, T. C.; Liopo, A. V.; Sinani, V. A.; Shim, B. S.; Motamedi, M.; Wicksted, J. P.; Kotov, N. A. Stimulation of Neural Cells by Lateral Currents in Conductive Layer-by-Layer Films of Single-Walled Carbon Nanotubes. *Adv. Mater.* **2006**, *18*, 2975–2979.
27. Cogan, S. F. Neural Stimulation and Recording Electrodes. *Annu. Rev. Biomed. Eng.* **2008**, *10*, 275–309.

28. Kotov, N. A.; Winter, J. O.; Clements, I. P.; Jan, E.; Timko, B. P.; Campidelli, S.; Pathak, S.; Mazzatenta, A.; Lieber, C. M.; Prato, M.; *et al.* Nanomaterials for Neural Interfaces. *Adv. Mater.* **2009**, *21*, 3970–4004.
29. Malarkey, E. B.; Parpura, V. Carbon Nanotubes in Neuroscience. *Brain Edema XIV* **2010**, *106*, 337–341.
30. Jan, E.; Hendricks, J. L.; Husaini, V.; Richardson-Burns, S. M.; Sereno, A.; Martin, D. C.; Kotov, N. A. Layered Carbon Nanotube-Polyelectrolyte Electrodes Outperform Traditional Neural Interface Materials. *Nano Lett.* **2009**, *9*, 4012–4018.
31. Luo, X.; Weaver, C. L.; Zhou, D. D.; Greenberg, R.; Cui, X. T. Highly Stable Carbon Nanotube Doped Poly(3,4-ethylenedioxythiophene) for Chronic Neural Stimulation. *Biomaterials* **2011**, *32*, 5551–5557.
32. Shim, B. S.; Zhu, J.; Jan, E.; Critchley, K.; Ho, S.; Podsiadlo, P.; Sun, K.; Kotov, N. A. Multiparameter Structural Optimization of Single-Walled Carbon Nanotube Composites: Toward Record Strength, Stiffness, and Toughness. *ACS Nano* **2009**, *3*, 1711–1722.
33. Shao, M. W.; Wang, D. B.; Yu, G. H.; Hu, B.; Yu, W. C.; Qian, Y. T. The Synthesis of Carbon Nanotubes at Low Temperature *via* Carbon Suboxide Disproportionation. *Carbon* **2004**, *42*, 183–185.
34. Lin, C. M.; Lee, Y. T.; Yeh, S. R.; Fang, W. L. Flexible Carbon Nanotubes Electrode for Neural Recording. *Biosens. Bioelectron.* **2009**, *24*, 2791–2797.
35. Zhou, Y. X.; Hu, L. B.; Gruner, G. A Method of Printing Carbon Nanotube Thin Films. *Appl. Phys. Lett.* **2006**, *88*, 123109.
36. Abadi, P. P. S. S.; Hutchens, S. B.; Greer, J. R.; Cola, B. A.; Graham, S. Buckling-Driven Delamination of Carbon Nanotube Forests. *Appl. Phys. Lett.* **2013**, *102*, 223103.
37. Shim, B. S.; Zhu, J. A.; Jan, E.; Critchley, K.; Kotov, N. A. Transparent Conductors from Layer-by-Layer Assembled Swnt Films: Importance of Mechanical Properties and a New Figure of Merit. *ACS Nano* **2010**, *4*, 3725–3734.
38. Zhu, J.; Shim, B. S.; Di Prima, M.; Kotov, N. A. Transparent Conductors from Carbon Nanotubes LbL-Assembled with Polymer Dopant with π-π Electron Transfer. *J. Am. Chem. Soc.* **2011**, *133*, 7450–7460.
39. Kam, N. W. S.; Jan, E.; Kotov, N. A. Electrical Stimulation of Neural Stem Cells Mediated by Humanized Carbon Nanotube Composite Made with Extracellular Matrix Protein. *Nano Lett.* **2009**, *9*, 273–278.
40. Jan, E.; Kotov, N. A. Successful Differentiation of Mouse Neural Stem Cells on Layer-by-Layer Assembled Single-Walled Carbon Nanotube Composite. *Nano Lett.* **2007**, *7*, 1123–1128.
41. Lovat, V.; Pantarotto, D.; Lagostena, L.; Cacciari, B.; Grandolfo, M.; Righi, M.; Spalluto, G.; Prato, M.; Ballerini, L. Carbon Nanotube Substrates Boost Neuronal Electrical Signaling. *Nano Lett.* **2005**, *5*, 1107–1110.
42. Malarkey, E. B.; Fisher, K. A.; Bekyarova, E.; Liu, W.; Haddon, R. C.; Parpura, V. Conductive Single-Walled Carbon Nanotube Substrates Modulate Neuronal Growth. *Nano Lett.* **2009**, *9*, 264–268.
43. Cellot, G.; Cilia, E.; Cipollone, S.; Rancic, V.; Sucapane, A.; Giordani, S.; Gambazzi, L.; Markram, H.; Grandolfo, M.; Scaini, D.; *et al.* Carbon Nanotubes Might Improve Neuronal Performance by Favouring Electrical Shortcuts. *Nat. Nanotechnol.* **2009**, *4*, 126–133.
44. Wang, X.; Xie, X.; Ku, G.; Wang, L. V.; Stoica, G. Noninvasive Imaging of Hemoglobin Concentration and Oxygenation in the Rat Brain Using High-Resolution Photoacoustic Tomography. *J. Biomed. Opt.* **2006**, *11*, 024015.
45. Keefer, E. W.; Botterman, B. R.; Romero, M. I.; Rossi, A. F.; Gross, G. W. Carbon Nanotube Coating Improves Neuronal Recordings. *Nat. Nanotechnol.* **2008**, *3*, 434–439.
46. Yoon, I.; Hamaguchi, K.; Borzenets, I. V.; Finkelstein, G.; Mooney, R.; Donald, B. R. Intracellular Neural Recording with Pure Carbon Nanotube Probes. *PLoS ONE* **2013**, *8*, e65715.
47. Jan, E.; Byrne, S. J.; Cuddihy, M.; Davies, A. M.; Volkov, Y.; Gun'ko, Y. K.; Kotov, N. A. High-Content Screening as a Universal Tool for Fingerprinting of Cytotoxicity of Nanoparticles. *ACS Nano* **2008**, *2*, 928–938.
48. Stieglitz, T.; Hansjorg, B.; Schuettler, M.; Meyer, J.-U. Micromachined, Polyimide-Based Devices for Flexible Neural Interfaces. *Biomed. Microdevices* **2000**, *2*, 283–294.
49. Kandel, E. R.; Schwartz, J. H.; Jessell, T. M. *Principles of Neural Science*, 4th ed.; McGraw-Hill: New York, 2000; p xli, 1414pp.
50. Franceschini, G. The Mechanics of Human Brain Tissue. Ph.D Thesis, University of Trento, 2006.
51. Merrill, D. R.; Bikson, M.; Jefferys, J. G. Electrical Stimulation of Excitable Tissue: Design of Efficacious and Safe Protocols. *J. Neurosci. Methods* **2005**, *141*, 171–198.
52. Wu, F.; Im, M.; Yoon, E. *A Flexible Fish-Bone-Shaped Neural Probe Strengthened by Biodegradable Silk Coating for Enhanced Biocompatibility*, Solid-State Sensors, Actuators and Microsystems Conference (TRANSDUCERS), 2011 16th International, 5−9 June 2011; 2011; pp 966−969.
53. Kozai, T. D.; Kipke, D. R. Insertion Shuttle with Carboxyl Terminated Self-Assembled Monolayer Coatings for Implanting Flexible Polymer Neural Probes in the Brain. *J. Neurosci. Methods* **2009**, *184*, 199–205.
54. Kozai, T. D.; Vazquez, A. L.; Weaver, C. L.; Kim, S. G.; Cui, X. T. *In Vivo* Two-Photon Microscopy Reveals Immediate Microglial Reaction to Implantation of Microelectrode through Extension of Processes. *J. Neural. Eng.* **2012**, *9*, 066001.
55. Kozai, T. D.; Marzullo, T. C.; Hooi, F.; Langhals, N. B.; Majewska, A. K.; Brown, E. B.; Kipke, D. R. Reduction of Neurovascular Damage Resulting from Microelectrode Insertion into the Cerebral Cortex Using *in Vivo* Two-Photon Mapping. *J. Neural. Eng.* **2010**, *7*, 046011.
56. Hu, S.; Maslov, K.; Wang, L. V. Second-Generation Optical-Resolution Photoacoustic Microscopy with Improved Sensitivity and Speed. *Opt. Lett.* **2011**, *36*, 1134–1136.
57. Xie, Z.; Jiao, S.; Zhang, H. F.; Puliafito, C. A. Laser-Scanning Optical-Resolution Photoacoustic Microscopy. *Opt. Lett.* **2009**, *34*, 1771–1773.
58. Aine, C. J. A Conceptual Overview and Critique of Functional Neuroimaging Techniques in Humans: I. MRI/FMRI and PET. *Crit. Rev. Neurobiol.* **1995**, *9*, 229–309.
59. Berg-Johnsen, J.; Langmoen, I. A. Isoflurane Hyperpolarizes Neurones in Rat and Human Cerebral Cortex. *Acta Physiol. Scand.* **1987**, *130*, 679–685.
60. Mamedov, A.; Kotov, N. A. Free-Standing Layer-by-Layer Assembled Films of Magnetite Nanoparticles. *Langmuir* **2000**, *16* (13), 5530–5533.
61. Kim, Y.; Zhu, J.; Yeom, B.; Di Prima, M.; Su, X.; Kim, J. G.; Yoo, S. J.; Uher, C.; Kotov, N. A. Stretchable Nanoparticle Conductors with Self-Organized Conductive Pathways. *Nature* **2013**, *500*, 59–63.